Journal of Glaciology

Article

Cite this article: Machguth H, Tedstone AJ, Mattea E (2023). Daily variations in Western Greenland slush limits, 2000–2021. *Journal of Glaciology* **69**(273), 191–203. https://doi.org/10.1017/jog.2022.65

Received: 19 January 2022
Revised: 7 July 2022
Accepted: 7 July 2022
First published online: 8 August 2022

Keywords:
Glacier hydrology; ice-sheet mass balance; melt-surface; polar firn; remote sensing

Author for correspondence:
Horst Machguth,
E-mail: horst.machguth@unifr.ch

cambridge.org/jog

Daily variations in Western Greenland slush limits, 2000–2021

Horst Machguth, Andrew J. Tedstone and Enrico Mattea

Department of Geoscience, University of Fribourg, CH-1700 Fribourg, Switzerland

Abstract

The marginal areas of the Greenland ice sheet develop streams and lakes each summer, documenting that surface runoff of meltwater is a major component of ice-sheet mass balance. Here we map the slush limit, a proxy for the extent of surface runoff, using daily MODIS data for the years 2000–2021. We develop an automated algorithm capable of detecting daily slush limits, provided sufficient image quality. The algorithm is applied to the ice sheet's western flank (61.7 °N to 76.5 °N). We find significant increasing trends in maximum slush limits until the year 2012, but not thereafter. We show that the slush limit typically rises quickly early in the ablation season but stabilizes before melting ceases. The data provide evidence that upward migration of surface runoff in summer 2012 stopped early at the upper margin of the ice slabs. These thick and continuous ice layers are located close to the surface, in the firn, and impede percolation of melt into deeper pore space. Had the ice slabs extended higher, the summer 2012 provided sufficient energy to raise the slush limit by another ∼300 m in elevation.

1. Introduction

Surface melt is being observed at increasingly higher elevations on the Greenland ice sheet (e.g. Nghiem and others, 2012; McGrath and others, 2013) and meltwater discharge has increased (Ahlstrøm and others, 2017). The observations underline that melt plays a dominant role in ice-sheet decline (Enderlin and others, 2014; van den Broeke and others, 2016). In total, 50–60% of current mass loss is attributed to increased surface melt (van den Broeke and others, 2016; Team IMBIE, 2020); the rest is mostly due to calving.

Meltwater generated at the ice-sheet surface either runs off or gets retained in snow and firn. Only meltwater that runs off contributes to mass loss. Consequently, it is of scientific interest to quantify the extent of the runoff area, that is the area where at least a fraction of the meltwater runs off and finds its way into the oceans. The runoff area's upper margin is typically labeled runoff limit (e.g. Pfeffer and others, 1991; Reeh, 1991; Braithwaite and others, 1994). The runoff limit is generally located in the accumulation area (Shumskii, 1955, 1964). The same author shows that runoff takes place where either (i) the refreezing capacity of the firn is smaller than the latent heat contained in melt and rain, or (ii) the sum of melt and rain exceeds a certain fraction of firn pore space.

Downslope from the runoff limit follows a zone where runoff is already substantial but its annual sum is clearly smaller than total accumulation. This zone has received limited attention in the literature and lacks established terms. The closest equivalents might be the slush limit (Müller, 1962), the slush line (Greuell and Knap, 2000) or the visible runoff limit (Tedstone and Machguth, 2022). All of these terms refer to water or runoff becoming visible at the surface. However, visible *surface discharge* develops only in accumulation areas where the refreezing capacity of the firn is not exhausted but there is insufficient pore space to accommodate melt and liquid precipitation (Shumskii, 1955). If pore space suffices but not refreezing capacity, runoff will take place *inside the firn* (Shumskii, 1955), with little or no visible expression on the surface. Both modes of runoff involve an aquitard that guides lateral motion of water: runoff inside the firn follows high firn densities near the pore close-off depth (tens of meters below the surface; Miller and others, 2018, 2020), while surface runoff is guided by low-permeability icy firn or thick near-surface ice layers (lying on top of otherwise porous firn; Machguth and others, 2016; Leone and others, 2020), termed ice slabs (MacFerrin and others, 2019).

On Greenland, the geographical extents of both modes of meltwater runoff depend on annual amounts of snow fall (MacFerrin and others, 2019) and have limited overlap (Tedstone and Machguth, 2022). Runoff inside the firn prevails where firn aquifers are present (Forster and others, 2014; Koenig and others, 2014). Aquifers have been mapped using Operation IceBridge radar (Miège and others, 2016).

Surface discharge on the ice sheet has been studied already by the US military (ACFEL, 1947; Holmes, 1955) and in the context of hydropower projects (Thomsen and others, 1989). Recent remote-sensing applications have focused on supraglacial lakes (e.g. Box and Ski, 2007; Miles and others, 2017) and mapping of surface streams (e.g. Yang and others, 2015, 2019).

Few studies have explicitly (Holmes, 1955) or implicitly (Poinar and others, 2015; Yang and others, 2019) addressed the runoff limit. Tedstone and Machguth (2022) investigated the visible runoff limit, over the entire ice sheet and most of the satellite era. They define the visible runoff limit as the highest location where supraglacial drainage networks are seen in optical

satellite imagery. Using Landsat, they show that Greenland's visible runoff area has increased by 29^{+6}_{-8} % since 1985. When compared to Miège and others (2016), the study also shows that surface runoff exceeds aquifer discharge by area.

The Landsat satellites provide one of the oldest remote-sensing archives suited to map visible runoff limits. High spatial resolution allows recognizing individual runoff features. The low temporal resolution, however, limits insight into annual evolution of visible runoff extent. Better suited to obtain such information are the Advanced Very High Resolution Radiometer (AVHRR) or the Moderate Resolution Imaging Spectrometer (MODIS). Both sensors provide daily global coverage, at the cost of relatively low spatial resolution.

Greuell and Knap (2000) demonstrated that AVHRR imagery (1.1 km resolution at nadir) is suitable for detecting the seasonal evolution of the 'slush line', which they consider a proxy for abundant surface runoff. The slush line refers to the uppermost occurrence of *slush*, which is snow with all pore space water-filled (Cogley and others, 2011). Holmes (1955) distinguishes between white slush (slush covered by unsaturated snow) and blue slush, that is a fully water-saturated snowpack which appears blue at the surface. In line with Greuell and Knap (2000) we here refer to slush as 'blue slush' which is easily recognizable by eye and from space.

This study builds on the work by Greuell and Knap (2000) by using MODIS to chart the evolution of the daily slush limit over the melt seasons. Instead of slush line we use the term slush limit Υ_S, coined by Müller (1962) to denote the uppermost *visible* appearance of 'material that is water saturated' (Benson, 1996). We develop an automated algorithm able to reliably detect the slush limit Υ_S at daily resolution, for most of Greenland's west coast from 2000 to 2021. We use the output of the algorithm to evaluate whether the rise of Υ_S follows identifiable patterns or differs strongly between melt seasons or regions. Finally, we quantify how annual maximum slush limits max Υ_S have evolved over time.

2. Study area

We focus on the western flank of the Greenland ice sheet where surface runoff is common (e.g. Holmes, 1955; Thomsen and others, 1989). The study domain comprises latitudes from 61.7 °N to 76.5 °N, or ∼1700 km in north-south direction. Toward its very south and north, the study area borders with regions where firn aquifers exist (Miège and others, 2016).

3. Data

The MODIS is a multispectral sensor (36 spectral bands) aboard the Aqua and Terra satellites. The satellites were launched in 1999 and 2002. The sensors provide at least daily coverage of each point on Earth at spatial resolutions ranging from 250 to 1000 m, depending on spectral band.

Here we use the data products MOD10A1 (MODIS/Terra Daily Snow Cover at 500 m resolution, version 6.0; Hall and Riggs, 2016) and MOD09GA (MODIS/Terra Surface Reflectance Daily at 500 m, version 6.0; Vermote and Wolfe, 2015). We use daily tiles from day-of-year 120 (29 or 30 April) to 280 (6 or 7 October), covering west Greenland and the entire MODIS era (2000–2021). All scenes are used, regardless of their percentage of cloud cover.

In addition to the MODIS data, we use the Arctic DEM Release7 (100 m resolution mosaic, v.3.0; Porter and others, 2018) and the outlines of the Greenland ice sheet according to Rastner and others (2012). In the analysis of derived Υ_S we utilize all available (2009 to present) hourly records of air temperature T_a measured at the PROMICE automatic weather stations (AWS) KAN_U (1840 m a. s. l.; 67.000 °N, 47.025 °W) and KAN_M (1270 m a. s. l.; 67.067 °N, 48.836 °W) (van As and others, 2011; Fausto and van As, 2019). Furthermore, we use T_a measured at the GC-Net station Dye-2 at ∼2120 m a.s.l., 66.480 °N, 46.279 °W (Steffen and Box, 2001).

4. Methods

Our approach to detect Υ_S is inspired by Greuell and Knap (2000) who used AVHRR imagery to detect slush lines during 1990–1997 for central western Greenland. Greuell and Knap (2000) use the term *slush line* to emphasize that the rather coarsely resolved AVHRR images (1.1 km at nadir) do not allow to directly map runoff. Their approach focuses on detecting the elevation where spatial variability of surface albedo transitions from low to high. Low spatial variability of surface albedo indicates the monotonous snow covered surface above the slush line. Higher variability of albedo is indicative of a surface where the bright snow cover is intersected with dark meltwater streams, lakes and slush fields.

Our algorithm deviates from Greuell and Knap (2000) by (i) being designed for application to MODIS, (ii) being automated and (iii) incorporating normalized difference water index for ice ($NDWI_{ice}$; Yang and Smith, 2013) as an additional detection criterion.

4.1. Preprocessing

4.1.1. Surface albedo from MOD10A1

The *snow_albedo_daily_tile* data from MOD10A1 (in the following simply referred to as MOD10A1) are stitched together, then reprojected to a Polar Stereographic projection (EPSG:3413) using nearest neighbor interpolation and finally cropped to the study area.

Initially all non-albedo values and clouds in MOD10A1 are masked. Subsequently, the scenes are filtered because the data (i) are subject to residual cloud effects (such as clouds or their shadows retained as albedo values) and (ii) contain frequent artifacts (with a stripy appearance) where albedo α is much lower than the surrounding grid cells (cf. Box and others, 2012).

Albedo values are masked out if at least one of the following three conditions is fulfilled: (i) $\alpha < 12\%$, (ii) $\alpha > 90\%$ and (iii) $|\alpha - \alpha_{11days}| \geq 30\%$. The last condition states that α of each individual pixel is compared to its median albedo α_{11days} over an 11-day buffer (5 days before and 5 days after the scene under investigation, excluding the day under investigation). The 11-day buffer is inspired by the MOD10A1 filtering applied by Box and others (2012).

4.1.2. $NDWI_{ice}$ from MOD09GA

We calculate the Normalized difference water index for ice ($NDWI_{ice}$; Yang and Smith, 2013) using the red (620–670 nm) and blue (459–479 nm) bands of the MODIS MOD09GA daily surface reflectance product:

$$\mathrm{NDWI_{ice}} = \frac{\mathrm{Blue} - \mathrm{Red}}{\mathrm{Blue} + \mathrm{Red}}. \quad (1)$$

Values of the resulting grids range from 1 to –1. Google Earth Engine (Google Inc) is used to process Daily $NDWI_{ice}$ mosaics corresponding to the whole study area.

4.1.3. Digital elevation model

The Arctic DEM is adjusted to represent elevation above the EGM2008 geoid, and is downsampled to the same grid and spatial extent as the preprocessed MOD10A1 and MOD09GA data. Using the ice-sheet mask by Rastner and others (2012), all DEM values outside the ice sheet are masked.

https://doi.org/10.1017/jog.2022.65 Published online by Cambridge University Press

4.2. Calculating the standard deviation of surface albedo

Greuell and Knap (2000) used the standard deviation of albedo (σ_α) to distinguish areas of high and low spatial variability of albedo. They calculated spatial variability, for each day and pixel, as σ_α of a square of 5 by 5 pixels. We base our detection of Y_S on the same metric but calculate σ_α differently.

Standard deviation of albedo is calculated based on preprocessed MOD10A1. Each pixel gets attributed a σ_α which is calculated along lines of pixels to optimize computational efficiency. Standard deviation is calculated over lines of 11 pixels in length with the pixel under consideration centered. The scanning is done around each pixel in the vertical and in the horizontal, resulting in two arrays of standard deviation. The final σ_α of each pixel is calculated as the average of its vertical and horizontal standard deviation. We chose a scan window of 11 pixels because of being similar in width to 5 AVHRR pixels ($\approx$ 5.5 km at nadir). For any pixel, σ_α is only calculated when horizontally and vertically a minimum of eight out of 11 pixels contain valid α. Otherwise the pixel value is masked. This condition automatically creates a small buffer around masked areas (e.g. ice-free terrain, clouds). The effect is desirable because MOD10A1 close to such regions is often unreliable (e.g. cloud shadows).

4.3. Finding slush limit candidates

The slush limit is the elevation where σ_α falls below a certain threshold (Greuell and Knap, 2000). Using a threshold in σ_α as the sole criteria for detecting Y_S, however, leads to a large percentage of erroneous detections. Hence, further criteria are needed (Greuell and Knap, 2000). Our approach is grouped around the central premise of a threshold in σ_α. We even found the threshold of 1.25% identified by Greuell and Knap, to perform well on the MOD10A1 derived grids of σ_α. However, all other conditions were developed independently. In the following, we first explain the basic workflow of the algorithm and then detail our set of conditions applied to find Y_S.

The search for daily Y_S is done along 83 longitudinal stripes. These stripes have a north-south extent of 20 km. Grid cells that fall into a stripe are grouped in 20 m elevation bins. In the following, we label the nth elevation bin $z_c(n)$.

For each day and stripe we aim at identifying the elevation bin that corresponds to Y_S. For a given day and stripe, the algorithm starts searching for Y_S when <40% of the grid cells are cloud covered. The following parameters are calculated for each $z_c(n)$ based on all grid cells that fall into that bin: (1) median σ_α ($M_{\sigma\alpha}$), (2) mean α (μ_α), (3) the 95th percentile of $NDWI_{ice}$ ($NDWI_{95th}$) and (4) mean elevation (μ_z). These parameters are subsequently used to determine whether elevation bins can be considered candidates for Y_S.

The algorithm scans through all elevation bins. An elevation bin $z_c(i)$ is retained as a candidate for Y_S if it fulfills *all* of a set of seven conditions. Below we first list the seven conditions, followed by detailed explanations.

1. $z_c(i)$ is at least seven elevation bins (=140 m) below the uppermost elevation bin, and at least 140 m above the lowermost elevation bin.
2. Cloudiness (i.e. percentage of masked grid cells) $\leq$ 25% for all seven elevation bins above and below $z_c(i)$.
3. All seven elevation bins above $z_c(i)$ have $M_{\sigma\alpha} < 1.25\%$ AND at least one of the four bins below $z_c(i)$ has $M_{\sigma\alpha} > 1.65\%$ AND all four bins below $z_c(i)$ have $M_{\sigma\alpha} > 1.25\%$
4. The mean of the μ_α of the five elevation bins above $z_c(i)$ is larger than the mean of the μ_α of the seven elevation bins below.
5. The mean of the μ_α of the seven elevation bins below $z_c(i)$ is smaller than 0.72.
6. The mean of the μ_α of $z_c(i)^{+5\,\text{bins}}_{-7\,\text{bins}}$ is larger than 0.52.
7. The mean of the $NDWI_{95th}$ of the seven $z_c(n)$ below $z_c(i)$ is at least 0.0075 larger than the mean $NDWI_{95th}$ of the seven $z_c(n)$ above $z_c(i)$.

Condition 1 guarantees that an elevation bin is not too close to the ice margin or the uppermost bin (the algorithm evaluates each elevation bin based on up to seven bins directly above and below). Condition 2 prohibits any detection of Y_S in the vicinity of larger clouded areas (prone to erroneous α, σ_α and $NDWI_{ice}$).

Condition 3 is key as it defines the possible positions of Y_S; all subsequent conditions serve to either confirm or reject suggested positions. The third condition evaluates where spatial variability of α drops below the threshold value. Figure 1 exemplifies this drop in $M_{\sigma\alpha}$. However, the algorithm has to deal with various realizations of Y_S that are often not as obvious as in Figure 1. Actual Y_S are characterized by low $M_{\sigma\alpha}$ over broad elevation ranges, starting directly above Y_S (condition 3 – all *seven* elevation bins above $z_c(i)$ have $M_{\sigma\alpha} < 1.25\%$). Below Y_S, $M_{\sigma\alpha}$ sometimes remains elevated over larger distances (cf. Fig. 1), sometimes drops off over relatively short distances (condition 3 – only *four* bins below $z_c(i)$ need to have $M_{\sigma\alpha} > 1.25\%$). Finally, there needs to be a certain contrast in $M_{\sigma\alpha}$, otherwise there is increased risk of erroneous detection (condition 3 – at least one of the four bins below $z_c(i)$ has $M_{\sigma\alpha} > 1.65\%$).

It would be desirable to formulate condition 3 more strictly. The condition expects $M_{\sigma\alpha} < 1.25\%$ over a range of seven elevation bins above a potential Y_S. In reality, spatial variability of surface albedo is consistently low for all elevations above Y_S. Quality issues in the MOD10A1 data played a role when formulating conditions. An elevation interval of seven bins was chosen because highest elevations are frequent subject to spurious grid-like or banded artifacts in MOD10A1 that let $M_{\sigma\alpha}$ rise above 1.25%.

Condition 4 searches for a change in μ_α, which is the second key-characteristic of Y_S. Conditions 5 and 6 constrain the search to a certain range of μ_α. Very high values of α typically do not occur directly above Y_S. Very low values directly below indicate the presence of a bare ice surface, not typically to be found at Y_S. The search window is more narrow above than below a potential Y_S (five vs. seven elevation bins). This choice was made as the area directly above was found to be particularly indicative of potentially erroneous detections. While changes in μ_α are a key indicator of the location of Y_S (Greuell and Knap, 2000), conditions 4–6 are deliberately kept vague: The threshold in condition 4 is dynamic; conditions 5 and 6 define a wide interval of μ_α (0.52–0.72). Formulating exact and narrow thresholds would limit large-scale applicability of the algorithm and conflicts with limitations in data quality.

Surface water is more abundant below Y_S. We introduced a change in $NDWI_{ice}$ as the third major characteristic of Y_S. Several statistics were tested to optimize condition 7 and we found the change of the 95th percentile of $NDWI_{ice}$ to be the strongest indicator. Nevertheless, differences are often small and a rather low threshold of 0.0075 was chosen. Condition 7 reduces the number of erroneous detections and removes weakly expressed slush limits. The latter typically occur early in the melt season at low elevations and leave no expression in $NDWI_{ice}$ values.

4.4. Filtering of slush limit candidates

The algorithm sometimes detects more than one candidate for Y_S on a given day and stripe. In such a case only the candidate with the highest μ_α (mean over seven elevation bins below and above a candidate) is retained. Remaining candidates for Y_S require filtering to remove false positives (Fig. 2). We apply an automated approach in two stages.

https://doi.org/10.1017/jog.2022.65 Published online by Cambridge University Press

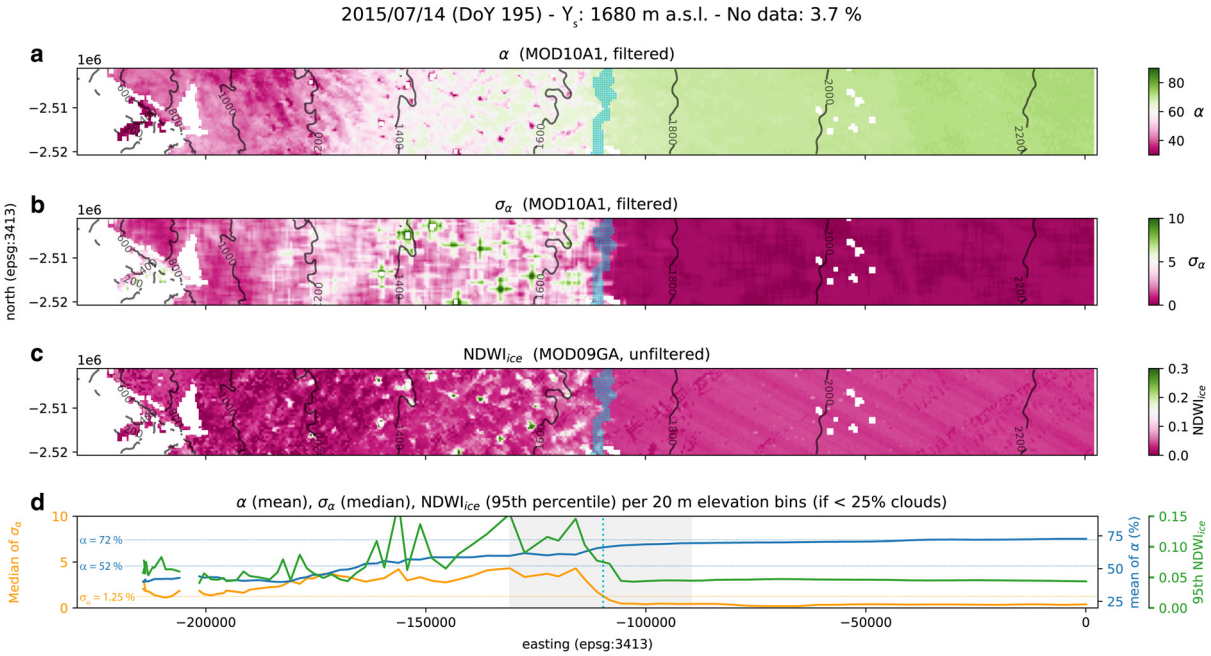

Fig. 1. Example of a slush limit Y_S as mapped on 14 July 2015 close to 67 °N. The detected Y_S (20 m elevation bin) is shaded in blue in subplots (a) to (c). (a) Filtered MOD10A1 albedo α in %. (b) Standard deviation of albedo (σ_α; in %) calculated along horizontal and vertical lines of pixels. (c) $NDWI_{ice}$ calculated from MOD09GA. (d) Median of σ_α (%), mean of α (%) and 95th percentile of $NDWI_{ice}$ calculated for all 20 m elevation bins. Gaps in the curves are where cloudiness exceeds a quarter of the gridcells in an elevation bin. The vertical dotted cyan line indicates the chosen Y_S; gray shading illustrates the maximum width (± 7 elevation bins) of the search window used to detect Y_S. Horizontal lines illustrate thresholds for α (in blue) and for σ_α (in orange). Threshold values are indicated on the figure.

In a first stage we filter the detections of the year with the highest Y_S. For all latitudinal stripes this is the year 2012 (see Section 5). In each latitudinal stripe we search for conflicts between the n available candidates. We examine all $(n(n-1)/2)$ pairs of candidates within the stripe: we define as conflicting all pairs where Y_S decreases substantially (> 45 m). Then, the candidate with the most conflicting pairs is excluded from the sample of candidates. The procedure is repeated until no conflicts are left within the latitudinal stripe. All excluded candidates are labeled invalid.

The filtering for conflicts is highly efficient in detecting outliers that are substantially higher or lower than its neighbors. However, the approach can only test whether the last candidate in a certain stripe falls substantially below its precursors. Any large positive deviation does not create a conflict. For this reason, the last valid candidate of each stripe needs separate filtering (thereby *valid* refers to having passed filtering for conflicts). We initially test whether the last valid candidate is substantially higher (> 95 m) than its valid precursor. If the rate of rise between the second last and the last candidate is also high (> 9.5 m d^{-1}), then the candidate is considered suspicious. Once a suspicious candidate has been found, the algorithm scans for valid candidates that fall into a window four stripes wide both in direction south and north and $\pm$ 8 days around the date of the suspicious candidate. For each of the eight stripes that fall into the search window, the algorithm retains the valid candidate which is closest in time to the suspicious candidate (if there is any within the ± 8 days time window). Consequently, there are up to eight neighboring candidates that are consulted whether they support the suspicious candidate. If they fall within 75 m of elevation of the suspicious candidate, they are considered supporting. If there are fewer than two supporting candidates, then the suspicious candidate is labeled invalid.

In a second stage, we apply filtering to all years. Initially, all candidates of a given stripe are compared to the highest valid Y_S in the year of highest Y_S. Candidates that exceed the highest valid Y_S by more than 40 m are labeled invalid. The 40 m threshold is introduced as the detections made during summer 2012 might have missed the absolute peak in some cases. Furthermore, comparison to the year of highest Y_S is only carried out if for a given stripe the year of highest Y_S has at least four valid detections and if there is at least one detection after 15 July. All candidates that pass the comparison to the year of highest Y_S are then filtered identical to filtering in stage 1 (described above).

4.5. Annual maximum slush limits

Deriving annual maximum slush limits $\max Y_S$ is challenging because the evolution of Y_S varies strongly between years and regions (Section 5.3). We derive $\max Y_S$ per stripe and year as follows: (1) $\max Y_S$ are only calculated if $n \geq 5$ detections exist for the year/stripe combination under investigation. (2) All n detections are sorted according to elevation in descending order. (3) Then we assign $\sigma_1 = 0$ to the highest detection, followed by calculating the standard deviation σ_2 for the two highest detections, again followed by calculating σ_3 over the three highest samples, until the nth and lowest sample is reached (σ_n). (4) We search local minima σ_i in the array of σ values, i.e. $\sigma_{i-1} \geq \sigma_i < \sigma_{i+1}$ (thereby σ_1 is always treated as a minimum). (5) Only σ_i are retained which fulfill the condition $\sigma_i \leq 25$ m (6) The σ_i with the highest standard deviation is then considered $\max Y_S$.

The highest σ_i corresponds to the largest group of Y_S whose standard deviation is still acceptable. The approach prefers larger groups of similar Y_S over isolated peaks (Fig. 3). In years where Y_S does climb more or less continuously, σ_1 typically is the only σ_i and selected as $\max Y_S$. Groups of similar Y_S that lie far below the highest individual value are excluded by the condition $\sigma_i \leq 25$ m.

Calculated $\max Y_S$ can be too early in the melt season to be reliably considered annual maxima. We exclude all derived annual maxima which take place before 10 July. In case the maxima is based on a group of detections, we test whether the latest date of the group is after 10 July. If this is the case, the $\max Y_S$ is retained.

https://doi.org/10.1017/jog.2022.65 Published online by Cambridge University Press

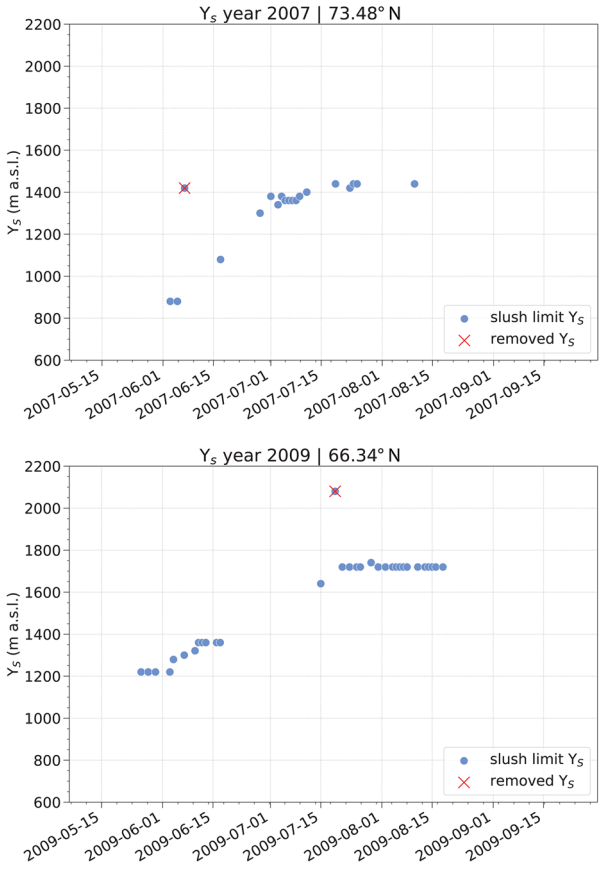

Fig. 2. Two examples of detected outliers among the slush limit candidates. Latitudes refer to the centers of the stripes.

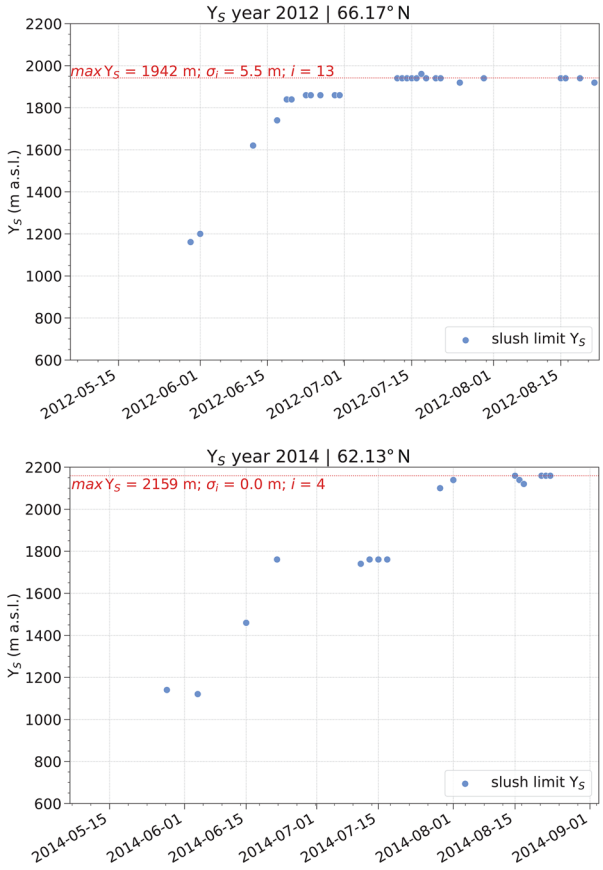

Fig. 3. Two examples of calculated annual maxima of the slush limit max Y_S. Latitudes refer to the centers of the stripes.

4.6. Comparison to Landsat-derived visible runoff limits

We compare Y_S to observations of the visible runoff limit Y_R identified from Landsat 30 m near-infrared imagery from 1985 to 2020 (Tedstone and Machguth, 2022). Briefly, the Landsat-derived observations are based on the extraction of supraglacial drainage networks to identify the locations at which visible meltwater runoff occurs. Landsat observations consist of up to 8000 retrievals of the visible runoff limit in any one Landsat scene (~ 8000 × 8000 pixels).

We compare our individual Y_S with Y_R. As Landsat retrievals use GIMPDEM (Howat and others, 2014) for elevation we first convert MODIS retrievals to use the same source. Then, for each Y_S, we identify all Landsat retrievals made within the MODIS stripe on the day of observation. If there are Landsat detections available, this usually yields at least several hundred visible runoff limit locations. We aggregate the Landsat locations by taking the median values of x, y and elevation. This yields a dataset of coincident Y_R and Y_S at the native spatial resolution of the MODIS retrievals.

Next, we filter the dataset to remove Y_R which are noisy or not comparable. (i) In each stripe, days on which the Y_R has an elevation median absolute deviation >100 m are removed (affecting 5.5% of observations). (ii) It is possible that at any given point in time, runoff features are detected on a Landsat scene situated below the actual Y_R, while no scene exists that covers the true Y_R. The highest Landsat detected runoff features could then be mistakenly considered the true Y_R. In such cases, the identified Y_R is located close to an edge of the scene. We therefore remove all paired observations whose Landsat retrieval was <500 pixels (~15 km) from the edge of the imaged scene. (iii) We filter out inter-comparisons where the MODIS coordinate falls outside of the WRS path/row bounding box of the Landsat scene being examined.

4.7. Meteorological conditions near the K-Transect slush limit

We investigate drivers of annual evolution of Y_S on the example of the K-Transect (67 °N), a region with good availability of meteorological observations (Section 3). We use cumulative positive degree hours (PDH) for a straightforward characterization of the energy input at the elevation of Y_S. While typically positive degree days are used (e.g. Reeh, 1991; Braithwaite, 1994), we here rely on PDH as hourly meteorological observations are available and the use of positive degree days at higher elevation on the ice sheet is subject to issues (van den Broeke and others, 2010).

Cumulative PDH over melt seasons 2009–2021 are calculated based on hourly records of air temperature T_a measured along the K-Transect at the PROMICE automatic weather stations (AWS) KAN_U (1840 m a. s. l.) and KAN_M (1270 m a. s. l.). For each year, the PDH at both stations are linearly interpolated to the elevation of the annual max Y_S.

5. Results

5.1. Overview

The algorithm determines 20 900 slush limit candidates, out of which the filtering keeps 19 800 (~95%) as valid Y_S.

On average, there are 900 Y_S per year or 10.8 per year and stripe. Detection is most frequent between 65.5 °N and 70.5 °N at 15–21 Y_S per year and stripe. For most of the remaining latitudinal stripes there are around 10 Y_S per year. Two intervals (71.5 – 72.25 °N and 75.25 – 76.5 °N) have only few Y_S.

https://doi.org/10.1017/jog.2022.65 Published online by Cambridge University Press

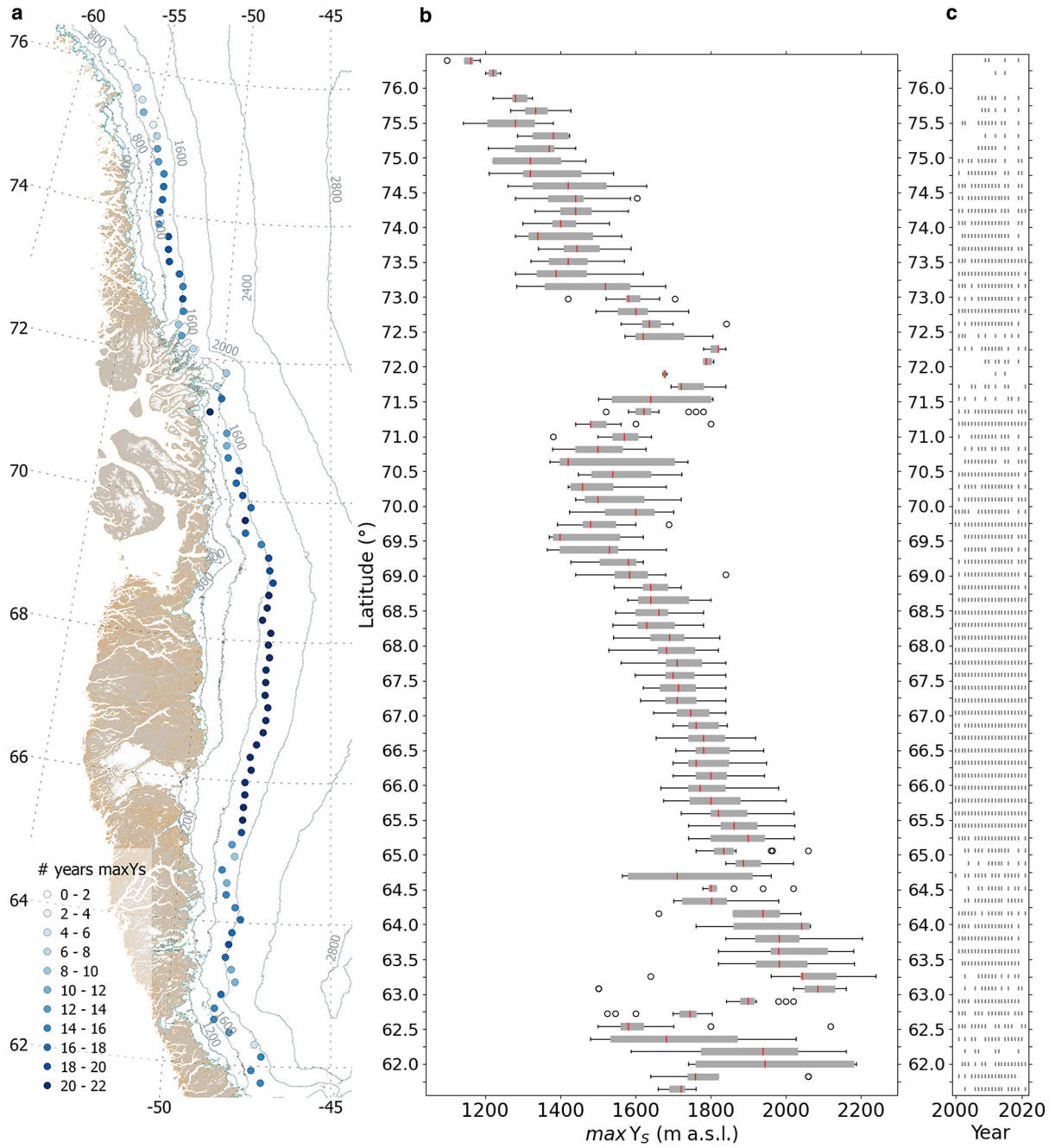

Fig. 4. Overview of maximum annual slush limits (max Y_S) retrieved for the years 2000–2021. (a) Greenland's west coast and location of median max Y_S. Colors indicate the number of successfully retrieved annual max Y_S. (b) Box plots of elevation (m a. s. l.) of all annual max Y_S. (c) Years with successful retrievals of max Y_S.

Maximum slush limits max Y_S were derived in 72% of all year/stripe combinations (1323 successful retrievals). Success rates vary between years and latitudes and are generally higher for latitudes 65.5 – 69.75 °N (Figs 4a and c) as well as in warm summers with relatively low cloud cover (e.g. 2012, 2019, cf. Fig. 5).

5.2. Spatial and temporal trends in annual maximum slush limits

Plotting max Y_S against latitude shows a clear decrease toward the north (Figs 4a and b). The median of max Y_S peaks at ~2080 m a.s.l. at around 63.25 °N and descends below 1300 m a. s. l. at the northern margin of our study area. Two regions divert from this general trend: (i) south of 63 °N max Y_S vary strongly with latitude and are on average lower than the adjacent stripes north, and (ii) 69.25–73 °N where max Y_S show no latitudinal trend.

Highest and lowest max Y_S in each stripe differ by 277 m on average. Inter-quantile distance and spread vary with latitude and peak in the south (Fig. 4b). Plotting max Y_S along the time axis (Fig. 5a) shows the highest median as well as absolute highest values in the year 2012; the lowest median is observed in the year 2001.

The irregular spatio-temporal distribution of retrieved max Y_S (Section 5.1) challenges the assessment of temporal trends in max Y_S. We calculate linear trends of annual median max Y_S over all latitudes (most affected by aforementioned issues) and for three regions where data coverage is more constant over time. These are 'central' (65.5–69.75 °N, 24 latitudinal stripes) where data coverage is optimal, 'south' (61.75–64.25 °N; 15 latitudinal stripes) and 'north' (72.5–75.0 °N; 13 latitudinal stripes). Furthermore, we assess trends over the full time period of the simulation as well as for the years 2000–2012 and 2013–2021.

https://doi.org/10.1017/jog.2022.65 Published online by Cambridge University Press

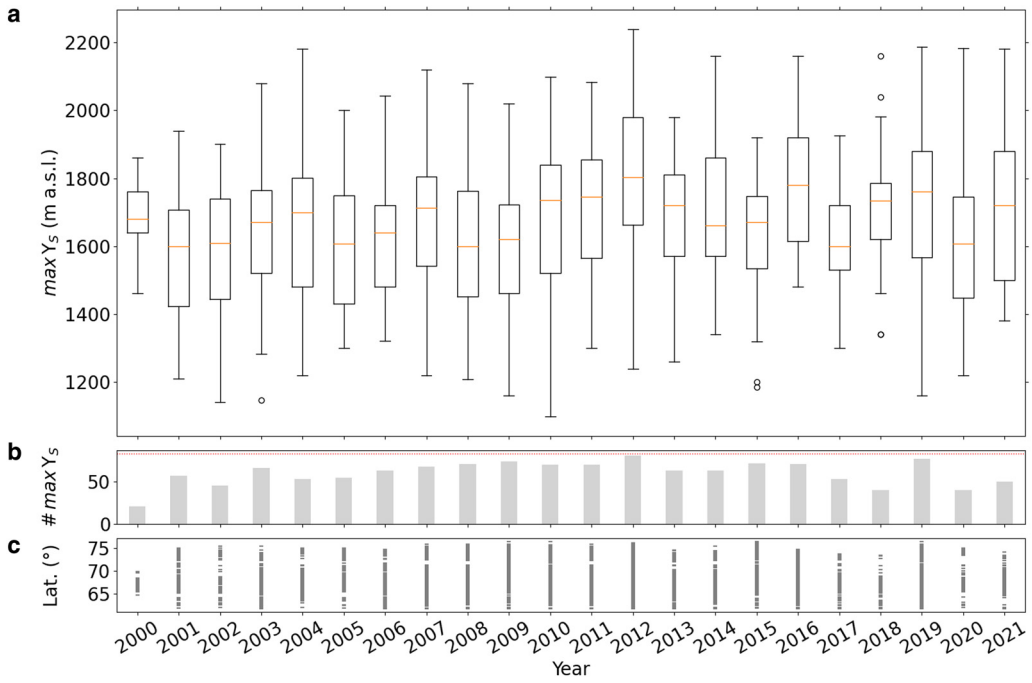

Fig. 5. Annual maximum slush limits (max Y_S) for the years 2000–2021. (a) Box plot of all max Y_S per year. (b) Number of latitudinal stripes with max Y_S. The dotted red line indicates the number of latitudinal stripes (83). (c) Latitudes of retrieved annual max Y_S.

Table 1. Linear regression of median annual max Y_S for the time periods 2000–2012, 2013–2021 and all years (2000–2021)

		Regions			
		South	Central	North	All stripes
2000–2012	Slope	**19.0**	**8.9**	**23.8**	**9.5**
	R^2	**0.38**	**0.36**	**0.93**	**0.32**
	p	**0.03**	**0.03**	**0.00**	**0.05**
2013–2021	Slope	*9.4*	*4.2*	*−6.3*	*−0.4*
	R^2	*0.05*	*0.03*	*0.06*	*0.00*
	p	*0.56*	*0.65*	*0.53*	*0.97*
All years	Slope	7.4	*2.9*	5.3	*3.5*
	R^2	0.17	*0.10*	0.17	*0.12*
	p	0.07	*0.15*	0.07	*0.11*

Slope is in m a^{-1}. Regressions significant at the 95% confidence level are highlighted in **bold**, at 90% in normal font. The remaining regressions are in *italic*.

These periods were defined based on Ryan and others (2019) who found a significant trend in bare-ice exposure of the ice sheet for the years 2000–2012 but not afterwards.

Table 1 summarizes the results of the regression analysis. All regions show significant positive trends at 95% confidence for 2000–2012. There are no significant trends for 2013–2021. Over the full time period we observe significant trends (at 90% confidence) for 'south' and 'north'.

5.3. Annual evolution of slush limits

The evolution of Y_S during individual summers shows substantial variability. We first assess differences by latitude, followed by the identification of characteristic temporal patterns.

Regionally averaged evolution of Y_S (Fig. 6) north of ~73 °N indicates a relatively uniform and gentle rise of Y_S. The observed melt season is relatively short. Further south (~64 to ~73 °N) the observed melt season is substantially longer. In May, the initial progression of Y_S is slow, followed by a steeper rise throughout June. Subsequently the rate of rise decreases and plateaus in early August. South of ~64 °N the rise of Y_S appears more monotonous. Again, in early August a plateau is reached.

Figure 6 illustrates how progression of Y_S in individual years differs from average behavior. There are examples where the progression of Y_S appears jagged or very long phases of absolutely linear 'growth' occur. There are also cases where Y_S is at max Y_S throughout the entire observed melt season. Such 'behavior' is generally associated with years that have extended phases without detection or very few detections. We therefore focus on years that have good data coverage to qualitatively identify reoccurring pattern.

With the exception of the southern-most region in Figure 6, the spread around the mean decreases toward the end of the melt season. Across most latitudes and in many years Y_S reaches a plateau where it remains until detection ceases in autumn (Fig. 6). Less frequently, Y_S continuously climbs until there is no more detection. A peculiar behavior of Y_S is observed at certain latitudes in the south. There, detected Y_S can switch suddenly from a lower to a substantially higher level. The reasons behind this behavior are not yet understood. It could be related to regions where surface discharge networks develop less clearly and runoff also occurs through aquifers. It might be that surface discharge develops quite abruptly when subsurface discharge is overwhelmed by high meltwater input.

5.4. Comparison to Landsat-derived visible runoff limits

We compared Y_S to observations of the visible runoff limit Y_R identified from Landsat 30 m near-infrared imagery from 1985 to 2020 (Tedstone and Machguth, 2022). Aggregating and filtering (Section 4.6) yields an inter-comparison dataset with 1335 paired observations, or ~ 7% of all 19 800 valid Y_S. Figure 7 shows the paired observations in a scatter plot, together with a linear regression. The latter is highly significant ($p < 0.0001$) and yields R^2 of 0.87.

5.5. Slush limit 'plateauing' and the summer of 2012

We observe frequent 'plateauing' of Y_S. To investigate the causes of this phenomenon, we utilize PDH data 2009–2021 from the

https://doi.org/10.1017/jog.2022.65 Published online by Cambridge University Press

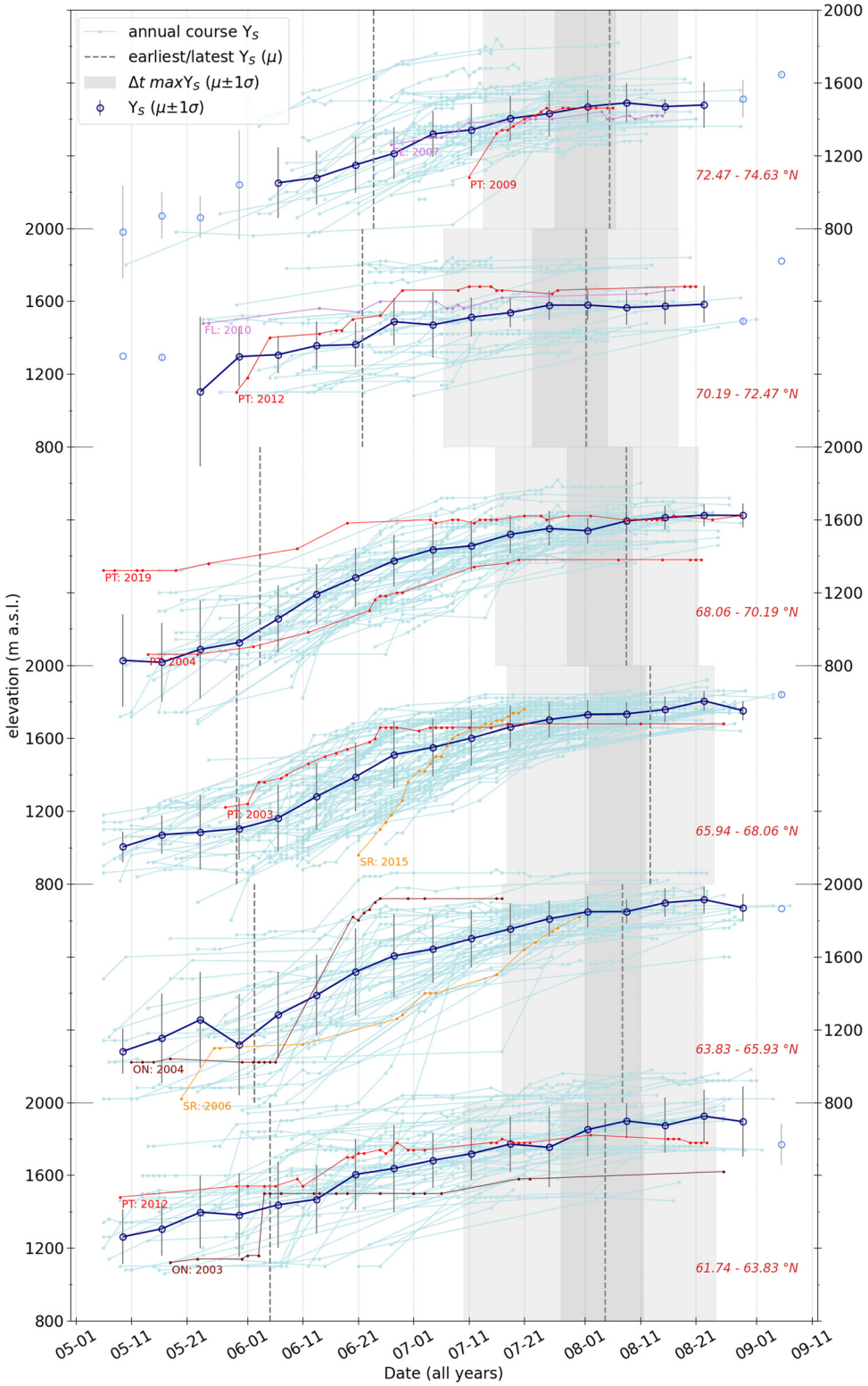

Fig. 6. Annual progression of the slush limit Y_S in six regions of the Greenland west coast. Each region comprises 12 latitudinal stripes. Navy blue lines and circles show average behavior calculated from all Y_S that fall into a region; pale blue circles denote averages based on <15 individual Y_S. Cyan lines and dots illustrate progression of Y_S in individual stripe/year combinations; for clarity only every 5th stripe/year combinations has been selected randomly. Slush limit progression in red to orange colors is selected manually to illustrate frequent behavior: FL, flat progression; PT, plateauing; SR, steep rise; ON, oscillation.

K-Transect (a region where the phenomenon is frequent). We find that 518 $\pm$ 152 PDH (average $\pm 1\sigma$) have occurred at the location of max Y_S by the time it is reached (Table 2). The minimum is 314 PDH (summer 2020), the maximum is 872 PDH (summer 2010). In the following, PDH$_{\Uparrow}$ designates the sum of PDHs consumed to bring Y_S to max Y_S.

We investigate whether the plateauing is caused by a lack of additional PDHs once max Y_S has been reached. We calculate PDH$_{\Rightarrow}$ as the amount of PDH that occur after when max Y_S is first reached and until T_a falls permanently below 0 °C. Excluding 2012, we find that PDH$_{\Rightarrow}$ is on average $\pm 1\sigma$ 142 $\pm$ 61 PDH. This corresponds to ~27% of PDH$_{\Uparrow}$.

In contrast, during the summer of 2012, PDH$_{\Rightarrow}$ amounted to 737 PDH. This value differs strongly from all other years (cf. Table 2) and is even substantially higher than the 530 PDH that occurred in 2012 before max Y_S was reached. Furthermore,

https://doi.org/10.1017/jog.2022.65 Published online by Cambridge University Press

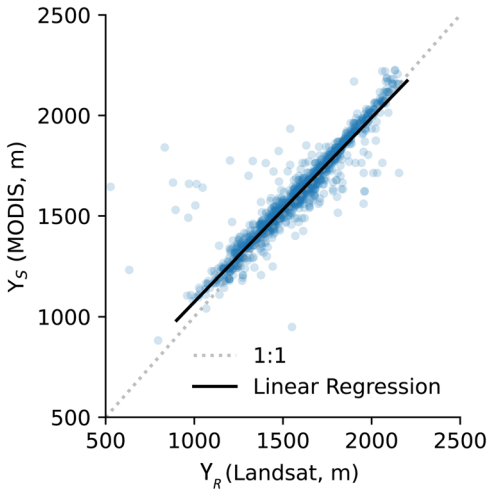

Fig. 7. Linear regression of Landsat-derived visible slush limits Y_R against MODIS-derived slush limits Y_S. Number of samples = 1335, slope of the linear regression is 0.857, $R^2 = 0.87$, $p < 0.0001$.

Table 2. Cumulative positive degree hours at the K-Transect before (PDH $_{\Uparrow}$) and after (PDH $_{\Rightarrow}$) the maximum slush limit (max Y_S) has been reached

Year	max Y_S		Plateau	PDH $_{\Uparrow}$	PDH $_{\Rightarrow}$
	m a.s.l.	DoY	Days	°C hr	°C hr
2009	1701	203	27	676	116
2010	1799	231	17	872	189
2011	1787	203	14	407	223
2012	*1841*	*190*	*19*	*530*	*737*
2013	1781	220	4	408	74
2014	1794	242	1	628	30
2015	1754	199	4	360	134
2016	1821	213	19	501	160
2017	1663	224	5	528	160
2018	1746	223	1	501	87
2019	1822	210	15	492	172
2020	1708	203	2	314	216
μ (all years)	1768	213	11	**518**	
σ (all years)	55	15	9	**152**	
μ (ex. 2012)					**142**
σ (ex. 2012)					**61**

All PDH values refer to the elevation of max Y_S in the respective years. The number of days between the first and last detection of max Y_S is labeled *plateau*. For max Y_S, the day of year (DoY) of its first detection and elevation (m a.s.l.) are given.

max Y_S was reached very early in the season, earlier than in any other year (Table 2).

6. Discussion

6.1. Performance of the algorithm

The data present a clear picture of the spatial and temporal evolution of Y_S along the western flank of the ice sheet and the 22 years from 2000 to 2021. The data also provide a detailed image of the annual evolution of Y_S in the majority of the latitudinal stripes and years. The degree of detail, however, varies across latitudes and years.

The total number of retrieved Y_S is limited by frequent cloudiness but also data quality. The latter is most obvious in the years 2000 and 2021 where MOD10A1 data are affected by severe striping and an erroneous cloud mask, respectively. It is unknown by how much the number of Y_S detection could be increased with an optimized algorithm. Dropping conditions increases detection but also the number of false positives. Consequently, stronger filtering would be needed. For example, before the $NDWI_{ice}$ threshold was added to the algorithm, the number of Y_S candidates was higher by ~40%. Compared to the final algorithm, the filtering (similar approach as in the final version) removed twice as many candidates, but a substantial number of false positives went undetected. Preference was given to a stricter algorithm that yields a somewhat smaller set of high-quality Y_S.

The filtering of the Y_S candidates works efficiently and there are virtually no obvious outliers left after filtering. Consequently, the data are here presented and used without manual removal of outliers. The filtering is relatively strict and the automated labeling of almost all outliers comes at the costs of (i) having spent a substantial amount of time on optimizing the filter and (ii) removal of some valid candidates.

Our algorithm records the rise of Y_S, it does not document lowering of Y_S. Decreasing Y_S could occur due to summer cold spells and at the end of the melt season. Indeed, candidates of Y_S often show a decrease in elevation at the end of summer. Such candidates are removed by the filtering for two reasons. Primarily, we consider upward migration of Y_S a clear indicator of a rise in the extent of surface runoff; decreasing Y_S are not necessarily indicative of a lowering limit of surface runoff. Lowering of Y_S, as recorded from MODIS data, is often related to summer or late ablation season snow fall events.

While able to mask the hallmarks of Y_S, snowfall does not immediately end the physical processes that take place around Y_S (i.e. water saturation in snow, lateral flow in the snow matrix and runoff in streams, cf. Fig. 8). The hydrologic system has substantial inertia as described by Holmes (1955). At ~66.3 °N/~47.8 °W they observed the surface hydrology at the runoff limit over the entire melt season of 1953. They report that melt ceased at 3 August 1953, but main rivers continued to flow at reduced discharge until 21 August when they had frozen over. We therefore believe that optical remote sensing is not optimally suited to observing decreases in slush limits. Secondly, and on a purely pragmatic level, filtering candidates of Y_S becomes easier when decreasing Y_S are removed.

6.2. Comparison to Landsat visible runoff limit and other data sets

The comparison to Landsat mapped visible runoff limits Y_R (Tedstone and Machguth, 2022) yields a very good agreement with 95% of differences < 135 m. This encouraging result is somewhat disturbed by outliers where Y_S and Y_R deviate by up to 1.2 km (Fig. 7). The character of these outliers was examined manually on a selection of 30 outliers. Absolute deviations of the selection range from 110 to 1170 m, random selection has been done separately for 15 strong outliers (absolute deviations > 200 m) and 15 moderate outliers (absolute deviations between 200 and 110 m). We found that 14 of the strong outliers are caused by issues in the comparison (see Section 5.4), not by failure of the Landsat or MODIS detection algorithms. One strong outlier was caused by failure of filtering of Y_S candidates. The causes of moderate outliers are more difficult to quantify. About half of them seem related to flawed comparisons, the remainder concerns vaguely expressed slush limits where Landsat Y_R is likely more accurate and a couple of cases where the reason is unclear. The analysis shows that it would be justified to remove most of the extreme outliers from the comparison of Y_S and Y_R. Consequently, the statistics presented in Section 5.4 and Figure 7 are conservative. Removal of the 32 outliers > 200 m that are not known to be caused by failure of the MODIS algorithm yields $R^2 = 0.96$ and a regression slope of 0.93 ($n = 1303$).

We find good qualitative agreement between max Y_S and AVHRR mapped slush lines of 1990 and 1995 by Greuell and Knap (2000) (Fig. 9). Greuell and Knap (2000) highlight the

https://doi.org/10.1017/jog.2022.65 Published online by Cambridge University Press

Fig. 8. The hole shown in the photo was dug on 29 July 2020 at a location (47.2391 °W, 66.9913 °N; ~1760 m a.s.l.) where a few days earlier (around July 22) a slush field had started to form (all pore space in the surface snow was water filled). Intense snowfall between 24 and 28 July had covered the newly formed slush field. While now hidden below the layer of fresh snow, water continued to flow slowly downhill. Depth of the hole 62 cm (equal to total snow depth), water depth 42 cm. The bottom of the hole and of the snow pack is formed by the ice slab which acts as aquitard and is at the location more than 10 m thick.

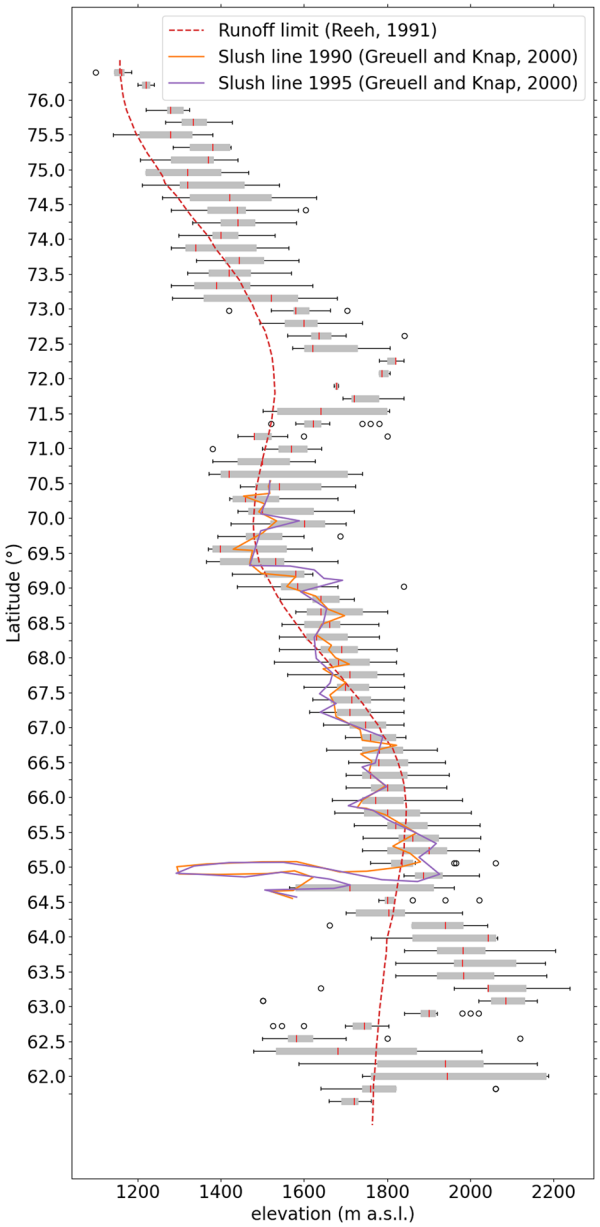

Fig. 9. Comparison of annual maximum slush limits to the *runoff limit* as calculated by Reeh (1991) as well as AVHRR derived *slush lines* (Greuell and Knap, 2000) for the years 1990 and 1995.

two years because of strong melting. Indeed, the comparison shows that the slush lines of the two strong melt summers of 1990 and 1995 coincide mostly with the median of max Υ_S. We restrict this comparison to a qualitative level because the slush lines according to Greuell and Knap (2000) needed digitizing from relatively low resolution figures and accuracy of their digital elevation model is poorly known.

Reeh (1991) used positive degree day modeling to calculate the snow line, the equilibrium line and the runoff limit for most of Greenland. Greuell and Knap (2000) argue that their slush lines are most representative for the runoff limit and compare their data to Reeh's (1991) runoff limits. We do the same (Fig. 9) and find that the two data sets agree well. The runoff limit according to Reeh (1991) shows fewer details because of the coarse resolution of the model input (mainly accumulation distribution and air temperatures) available at the time.

6.3. Slush limit, visible and actual runoff limit

The Landsat visible runoff limits agree well to MODIS Υ_S, but the question remains to what degree they represent the actual runoff limit, that is the highest elevation where a minimal fraction of melt finds a way to the ocean. Holmes (1955) wrote of 'white slush' that is hidden under a layer of unsaturated snow and thus typically invisible to optical remote sensing. While not measured directly by Holmes (1955), their study indicated that lateral runoff in white slush reached at least 4.2 km (2.6 miles) above the highest visible slush fields. Clerx and others (2022) directly measured lateral flow velocity inside the snow, in a shallow layer of meltwater on top of the ice slab. Multiplying measured velocities with a rough estimate of days per melt season where water can flow yields a value similar to Holmes (1955). Tedstone and Machguth (2022) note that their visible runoff limits are 10–20 m lower in elevation than the upper limit of the runoff area at the EGIG line (~69.7 °N, ~48.5 °W), as quantified for the years 2007 and 2008 by Humphrey and others (2012). Based on these references, we cautiously conclude that MODIS Υ_S provide a reasonably good estimate of the actual runoff limit. Compared to the latter, Υ_S are likely biased low by a few kilometers. This estimate refers to regions with well-developed ice slabs.

6.4. Temporal trends in maximum slush limit elevation

Our data show weak or insignificant trends in max Υ_S (Section 5.2) when focusing on the full time period. This appears to

https://doi.org/10.1017/jog.2022.65 Published online by Cambridge University Press

contradict Tedstone and Machguth (2022) who find a substantial increase in the visible runoff limit. However, they investigate 1985 to present, 15 years more than this study. They also show that the increase in the visible runoff limit levels off after the year 2012. The absence of a trend in $\max Y_S$ might also be perceived to be at odds with studies that charted the inland progression of supraglacial lakes (e.g. Howat and others, 2013; Gledhill and Williamson, 2017). Similar to Tedstone and Machguth (2022), these studies consider longer time periods. In addition, they exclude the most recent years (e.g. Howat and others, 2013, end with the year 2012).

Ryan and others (2019) assessed the extent of bare ice exposure on the entire Greenland ice sheet from 2001 to 2017. They found no significant linear trend in end-of-summer snowline elevation and bare ice extent over their full study period. In contrast, they observed a significant trend when focusing on 2000–2012. We observe a similar behavior of $\max Y_S$ with a significant rise until the year 2012. In the north and south of our study area $\max Y_S$ increased by $\sim 20\,\mathrm{m\,a^{-1}}$.

The emerging pattern of a relatively steep increase of $\max Y_S$ until 2012, followed by stagnation, is in broad agreement with the observed evolution of ice content in firn at the K-Transect (Rennermalm and others, 2021). A peak in ice content was measured directly after the series of intense melt years had peaked in 2012. Since then ice content has decreased. However, the analysis of Rennermalm and others (2021) ends with the year 2018, excluding the strong melt summer of 2019.

6.5. 'Plateauing' and the slush limit in the summer of 2012

We calculated PDH at K-Transect $\max Y_S$ to investigate reasons behind frequent 'plateauing' of Y_S. We find that 518 ± 152 PDH are consumed to bring Y_S to its annual maxima. There are no extreme outliers. Varying amounts of snow could be a reason for the differences between years: the more snow, the more melt is needed to fill the pore space until water becomes visible at the surface. Inaccuracies in the data (see below) likely also contribute to the differences. We calculate that $\sim$ 27% of total annual PDH (excluding the year 2012) occur after $\max Y_S$ has been reached. Apparently, this amount of PDH is insufficient to lift Y_S above $\max Y_S$ but suffices to stabilize Y_S, sometimes for more than a month.

It is beyond the scope of this study to investigate how the stabilization of Y_S exactly works. It is possible that, once the hydrologic network is established, the slush limit remains visible on MODIS imagery even with reduced water supply. As observed by Holmes (1955), meltwater mobilized earlier in the season contributes to maintaining late-season Y_S. PDH that occur late in the season likely assist in such processes. Alternatively, one might suggest that 'plateauing' of Y_S marks the upper extent of a near-surface aquitard, such as solid glacier ice or an ice slab. Indeed, Greuell and Knap (2000) observed that in three warm summers melting continued while their AVHRR-derived slush lines had already stopped at a certain elevation (roughly at 1720 m a.s.l. at the K-Transect). They suggested that this behavior is related to sudden changes in the density of the subsurface. In the following we discuss this hypothesis in the context of the 2012 melt season.

The year 2012 reached the highest $\max Y_S$ ($\sim$ 1840 m a.s.l. at the K-Transect; Table 2 and Fig. 5), but stands out even clearer in terms of PDHs at $\max Y_S$. There was an extraordinary sum of PDH that occurred after $\max Y_S$ had been reached (Table 2). Why did Y_S not rise any further, given abundant melt energy? There are either data issues or a physical reason for Y_S stagnating.

Along the K-Transect, all years have a high number of Y_S retrievals without substantial data gaps around the date when $\max Y_S$ is reached. There are years where detection of Y_S stops relatively early (among them the year 2012). Nevertheless, undetected rise in Y_S is unlikely because neighboring latitudes do not show marked increase of Y_S after detections along the K-Transect ceased. Estimated PDH rely on only two AWS and interpolation to $\max Y_S$ is done linearly. Still, errors in the interpolation are probably small because the elevation difference between $\max Y_S$ and the KAN_U AWS is < 140 m for all but one year. In the year 2012, $\max Y_S$ was directly at KAN_U. Consequently, we assume that uncertainties in PDH are of limited influence.

Spatial variations of firn properties, namely a decrease in ice content, are very likely to have stopped the 2012 rise in Y_S. At elevations below $\max Y_S$ the ice slab acted as near-surface aquitard, provoking visible runoff. At elevations $>$ $\max Y_S$ the ice slab is discontinuous or absent. In these areas meltwater percolated vertically into the porous firn rather than forming slush fields and streams. Our assumption is based on $\sim$40 firn cores, drilled at and above KAN_U in 2012, 2013 and later years (Machguth and others, 2016; MacFerrin and others, 2019; Rennermalm and others, 2021). Radar profiles from spring 2013 show the ice slab extending approximately as high as KAN_U (Machguth and others, 2016; MacFerrin and others, 2019).

6.6. Long-term trends in slush limit elevation

The year 2012 is the only year with clear evidence of firn properties controlling $\max Y_S$. Firn data from around $\max Y_S$ and before 2012 are very scarce. This makes it difficult to prove whether in other years before 2012 $\max Y_S$ was collocated with *'a sudden change in the density profile'* (Greuell and Knap, 2000). For the time period 1990–1995, Greuell and Knap estimated the 'abrupt change in the density profile' at $\sim$1720 m a.s.l. Since then, the 'sudden change in the density profile' has migrated upslope to 1840 m a.s.l. Greuell and Knap (2000) emphasize that positions of their slush lines are subject to an uncertainty of ± 2 km (furthermore, the DEM was of 2 km spatial resolution). Nevertheless, the increase of $\sim$120 m at the K-Transect appears substantial and might answer a question formulated by Greuell and Knap (2000), namely to what degree the location of the 'abrupt change in the density profile' varies as a function of climate.

How did the 'abrupt change in the density profile' look like in the early 1990s? Ice slabs of the western flank of the ice sheet are typically transient phenomena (Leone and others, 2020) in a warming climate. The climatic conditions preceding the measurements of Greuell and Knap are characterized by an extended period (1930 s to early 1990 s) of slight cooling (Van As and others, 2016; Cappelen, 2021). The slush limit of the early 1990s might have been associated with the upper margin of continuous glacial ice, not with ice slabs. Indeed, a radar profile from spring 2013 (Machguth and others, 2016; MacFerrin and others, 2019) shows the uppermost appearance of continuous ice (down to at least 20 m depth) at $\sim$1700 m a.s.l. At higher elevations, the ice slab overlies porous firn.

It is tempting to estimate the potential $\max Y_S$ of summer 2012 at the K-Transect. At the elevations of $\max Y_S$, the sum of PDH is 657 ± 159 at end of melt season (average $\pm 1\sigma$; all years excluding 2012). Using linear interpolation we find that in 2012 the same amount of cumulative PDH occurred at 2154 ± 82 m a.s.l. Assuming the ice slab would have extended to higher elevations, $\max Y_S$ could have risen $\sim$ 300 m above the observed $\max Y_S$ (1841 m a.s.l., cf. Table 2). This estimate is supportedby a total of 850 PDH measured in 2012 at the GC-Net station Dye-2 at $\sim$ 2120 m a.s.l., $\sim$60 km south of the K-Transect. Our analysis underlines the exceptional character of the summer 2012 and shows that surface runoff from deep within the current accumulation area can take place as soon as firn density profiles have become favorable.

https://doi.org/10.1017/jog.2022.65 Published online by Cambridge University Press

7. Conclusions

We designed an automated algorithm to detect the slush limit along most of the western margin of the Greenland ice sheet. The approach was applied to daily MODIS data covering the study area and all years of the MODIS record (2000–2021). We find very good agreement with visible runoff limits mapped from higher resolution Landsat data (Tedstone and Machguth, 2022).

Our results document spatial variations of the slush limit with high accuracy and yield good temporal detail. We observe frequent 'plateauing' of the slush limit, that is the slush limit stops rising clearly before the end of the melt season. While we find weak or absent trends in the slush limit over the entire time period, there is a clear and significant linear trend that peaks and ends in the year 2012.

Our algorithm is 'classical' in the sense that we do not rely on computer learning or artificial intelligence (AI). Advantages are replicability and potentially process understanding, disadvantages could be fewer detected slush limits and a higher number of false positives. There might be potential in exploring our concept in an AI framework.

Our data shed new light on the extraordinary characteristic of the summer of 2012. On the example of the K-Transect (67 °N) we showed that the rise of the slush limit, and thus also the extent of surface runoff, stopped early in the season at the upper margin of the ice slabs. If firn conditions would have allowed, the slush limit would have risen further, potentially up to 2154 ± 82 m a.s.l. While this number is still hypothetical, it underpins concerns about the future of the Greenland ice sheet.

Data and code availability. Code and output is available at https://doi.org/10.5281/zenodo.6892165. MODIS MOD10A1 and MOD09GA data products were downloaded from https://www.earthdata.nasa.gov/. The ArcticDEM Release 7 v3.0 is available at https://www.pgc.umn.edu/data/arcticdem/. PROMICE weather station data are available at https://dataverse.geus.dk/dataverse/AWS. GC-Net data were downloaded from https://www.envidat.ch/data-api/gcnet/.

Acknowledgements. This study is funded by the European Research Council (ERC) under the European Union's Horizon 2020 research and innovation programme (project acronym CASSANDRA, grant agreement No. 818994). We thank two anonymous reviewers and the editor for their valuable comments.

Author contributions. H.M. designed the study and carried out most of the analysis. A.T. contributed to study design, analysis and provided input data. Code was written by H.M. with contributions by A.T. and E.M. who designed and wrote code for the filtering approach. The study has been written by H.M. with contributions by A.T. and E.M.

References

ACFEL (1947) Report of Corps of Engineers observers on Project Snowman of Atlantic Division, ATC: investigation of construction and maintenance of airdromes on ice, 1947–1948. Technical report, Arctic Construction and Frost Effects Laboratory (ACFEL) – Engineer Research and Development Center.

Ahlstrøm AP, Petersen D, Langen PL, Citterio M and Box JE (2017) Abrupt shift in the observed runoff from the southwestern Greenland ice sheet. *Science Advances* **3**, e1701169. doi: 10.1126/sciadv.1701169

Benson CS (1996) Stratigraphic studies in the snow and firn of the Greenland ice sheet. Research Report 70, U.S. Army Snow, Ice and Permafrost Research Establishment.

Box JE and 5 others (2012) Greenland ice sheet albedo feedback: thermodynamics and atmospheric drivers. *The Cryosphere* **6**, 821–839. doi: 10.5194/tc-6-821-2012

Box JE and Ski K (2007) Remote sounding of Greenland supraglacial melt lakes: implications for subglacial hydraulics. *Journal of Glaciology* **53** (181), 257–265. doi: 10.3189/172756507782202883

Braithwaite R (1994) Degree day factor, energy balance and ablation in Greenland. In van der Meer JJM and Braithwaite RJ (eds), *Mass balance and related topics of the Greenland ice sheet*, volume 94 of *Open File Series*. Copenhagen, Denmark: Geological Survey of Greenland.

Braithwaite RJ, Laternser M and Pfeffer WT (1994) Variations of near-surface firn density in the lower accumulation area of the Greenland ice sheet, Pakitsoq, West Greenland. *Journal of Glaciology* **40**(136), 477–485.

Cappelen J (2021) Greenland – DMI historical climate data collection 1784–2020. Technical Report 21-04, Danish Meteorological Institute.

Clerx N and others (2022) In situ measurements of meltwater flow through snow and firn in the accumulation zone of the SW Greenland Ice Sheet. *EGUsphere* [preprint] doi: 10.5194/egusphere-2022-71

Cogley J and 10 others (2011) Glossary of glacier mass balance and related terms.

Enderlin E and 5 others (2014) An improved mass budget for the Greenland ice sheet. *Geophysical Research Letters* **41**, 866–872. doi: 10.1002/2013GL059010

Fausto R and van As D (2019) Programme for monitoring of the Greenland ice sheet (PROMICE): automatic weather station data. version: v03. doi: 10.22008/promice/data/aws.

Forster RR and 13 others (2014) Extensive liquid meltwater storage in firn within the Greenland ice sheet. *Nature Geoscience* **7**, 95–98. doi: 10.1038/ngeo2043

Gledhill LA and Williamson AG (2017) Inland advance of supraglacial lakes in north-west Greenland under recent climatic warming. *Annals of Glaciology* **59**(76pt1), 66–82. doi: 10.1017/aog.2017.31.

Greuell WB and Knap WH (2000) Remote sensing of the albedo and detection of the slush line on the Greenland ice sheet. *Journal of Geophysical Research* **105**(D2), 15567–15576. doi: 10.1029/1999JD901162

Hall DK and Riggs GA (2016) MODIS/Terra Snow Cover Daily L3 Global 500 m SIN Grid, Version 6, MOD10A1. doi: 10.5067/MODIS/MOD10A1.006.

Holmes CW (1955) Morphology and hydrology of the Mint Julep area, southwest Greenland. In *Project Mint Julep Investigation of Smooth Ice Areas of the Greenland Ice Cap, 1953; Part II Special Scientific Reports*, Arctic, Desert, Tropic Information Center; Research Studies Institute; Air University.

Howat IM, de la Peña S, van Angelen JH, Lenaerts JTM and van den Broeke MR (2013) Brief communication 'expansion of meltwater lakes on the Greenland ice sheet'. *The Cryosphere* **7**, 201–204. doi: 10.5194/tc-7-201-2013

Howat IM, Negrete A and Smith BE (2014) The Greenland Ice Mapping Project (GIMP) land classification and surface elevation data sets. *The Cryosphere* **8**, 1509–1518. doi: 10.5194/tc-8-1509-2014

Humphrey NF, Harper JT and Pfeffer WT (2012) Thermal tracking of meltwater retention in Greenland's accumulation area. *Journal of Geophysical Research* **117**, F01010. doi: 10.1029/2011JF002083

Koenig LS, Miège C, Forster RR and Brucker L (2014) Initial in situ measurements of perennial meltwater storage in the Greenland firn aquifer. *Geophysical Research Letters* **41**, 81–85. doi: 10.1002/2013GL058083

Leone R, Harper J, Meierbachtol T and Humphrey N (2020) Horizontal ice flow impacts the firn structure of Greenland's percolation zone. *The Cryosphere* **14**, 1703–1712. doi: 10.5194/tc-14-1703-2020

MacFerrin M and 13 others (2019) Rapid expansion of Greenland's low-permeability ice slabs. *Nature* **573**, 403–407. doi: 10.1038/s41586-019-1550-3

Machguth H and 9 others (2016) Greenland meltwater storage in firn limited by near-surface ice formation. *Nature Climate Change* **6**, 390–393. doi: 10.1038/nclimate2899

McGrath D, Colgan W, Bayou N, Muto A and Steffen K (2013) Recent warming at Summit, Greenland: global context and implications. *Geophysical Research Letters* **40**, 2091–2096. doi: 10.1002/grl.50456

Miège C (2016) Spatial extent and temporal variability of Greenland firn aquifers detected by ground and airborne radars. *Journal of Geophysical Research* **121**, 2381–2398. doi: 10.1002/2016JF003869

Miles KE, Willis IC, Benedek CL, Williamson AG and Tedesco M (2017) Toward monitoring surface and subsurface lakes on the Greenland ice sheet using Sentinel-1 SAR and Landsat-8 OLI imagery. *Frontiers of Earth Science* **5**, 58. doi: 10.3389/feart.2017.00058

Miller O and 7 others (2018) Direct evidence of meltwater flow within a firn aquifer in southeast Greenland. *Geophysical Research Letters* **45**, 207–215. doi: 10.1002/2017GL075707

Miller O and 10 others (2020) Hydrology of a perennial firn aquifer in southeast Greenland: an overview driven by field data. *Water Resources Research* **56**, 4–8. doi: 10.1029/2019WR026348

Müller F (1962) Zonation in the accumulation area of the glaciers of Axel Heiberg Island, N.W.T., Canada. *Journal of Glaciology* **4**, 302–311. doi: 10.3189/S0022143000027623

Nghiem SV and 8 others (2012) The extreme melt across the Greenland ice sheet in 2012. *Geophysical Research Letters* **39**, L20502. doi: 10.1029/2012GL053611

Pfeffer WT, Meier M and Illangasekare TH (1991) Retention of Greenland runoff by refreezing: implications for projected future sea level change. *Journal of Geophysical Research* **96**, 22117–22124. doi: 10.1029/91JC02502

Poinar K and 5 others (2015) Limits to future expansion of surface-melt-enhanced ice flow into the interior of western Greenland. *Geophysical Research Letters* **42**, 1800–1807. doi: 10.1002/2015GL063192

Porter C and 28 others (2018) 'ArcticDEM', Harvard Dataverse, V1. doi: 10.7910/DVN/OHHUKH.

Rastner P and 5 others (2012) The first complete inventory of the local glaciers and ice caps on Greenland. *The Cryosphere* **6**, 1483–1495. doi: 10.5194/tc-6-1483-2012

Reeh N (1991) Parameterizations of melt rate and surface temperature on the Greenland ice sheet. *Polarforschung* **59**, 113–128.

Rennermalm AK and 12 others (2021) Shallow firn cores 1989–2019 in southwest Greenland's percolation zone reveal decreasing density and ice layer thickness after 2012. *Journal of Glaciology* **68**(269), 431–442. doi: 10.1017/jog.2021.102

Ryan JC and 5 others (2019) Greenland ice sheet surface melt amplified by snowline migration and bare ice exposure. *Science Advances* **5**, eaav3738. doi: 10.1126/sciadv.aav3738

Shumskii PA (1955) *Osnovy Strukturnogo Ledovedeniya*. Moskva: Izdatel'stvo Akademii Nauk SSSR.

Shumskii PA (1964) *Principles of Structural Glaciology (Translated from the Russian by David Kraus)*. New York: Dover Publications .

Steffen K and Box JE (2001) Surface climatology of the Greenland ice sheet: Greenland Climate Network 1995–1999. *Journal of Geophysical Research* **106**(D24), 33951–33964. doi: 10.1029/2001JD900161

Team IMBIE (2020) Mass balance of the Greenland ice sheet from 1992 to 2018. *Nature* **597**, 233–239. doi: 10.1038/s41586-019-1855-2

Tedstone A and Machguth H (2022) Increasing surface runoff from Greenland's firn areas. *Nature Climate Change* **12**, 672–676. doi: 10.1038/s41558-022-01371-z

Thomsen HH, Thorning L and Olesen OB (1989) Applied glacier research for planning hydro-electric power, Illulissat/Jakobshavn, West Greenland. *Annals of Glaciology* **13**, 257–261.

van As D and 11 others (2011) Programme for Monitoring of the Greenland Ice Sheet (PROMICE): first temperature and ablation records. *Geological Survey of Denmark and Greenland Bulletin* **23**, 73–76. doi: 10.34194/geusb.v23.4876

van As D and 5 others (2016) Placing Greenland ice sheet ablation measurements in a multi-decadal context. *Geological Survey of Denmark and Greenland Bulletin* **35**, 71–74.

van den Broeke M and 7 others (2016) On the recent contribution of the Greenland ice sheet to sea level change. *The Cryosphere* **10**, 1933–1946. doi: 10.5194/tc-10-1933-2016

van den Broeke M, Bus C, Ettema J and Smeets P (2010) Temperature thresholds for degree day modelling of Greenland ice sheet melt rates. *Geophysical Research Letters* **37**, L18501. doi: 10.1029/2010GL044123

Vermote E and Wolfe R (2015) MOD09GA MODIS/Terra Surface Reflectance Daily L2G Global 1 km and 500 m SIN Grid V006. doi: 10.5067/MODIS/MOD09GA.006.

Yang K and 5 others (2015) River detection in remotely sensed imagery using Gabor filtering and path opening. *Remote Sensing* **7**(7), 8779–8802. doi: 10.3390/rs70708779

Yang K and 5 others (2019) Supraglacial rivers on the northwest Greenland ice sheet, Devon ice cap, and Barnes ice cap mapped using Sentinel-2 imagery. *International Journal of Applied Earth Observation and Geoinformation* **78**, 1–13. doi: 10.1016/j.jag.2019.01.008

Yang K and Smith LC (2013) Supraglacial streams on the Greenland ice sheet delineated from combined spectral-shape information in high-resolution satellite imagery. *IEEE Geoscience and Remote Sensing Letters* **10**(4), 801–805. doi: 10.1109/LGRS.2012.2224316

https://doi.org/10.1017/jog.2022.65 Published online by Cambridge University Press